Supporting Information

Ultrafine Ir nanoparticles anchored on carbon nanotubles as efficient bifunctional oxygen catalysts for Zn-air battery

Jianglian Wang, Mengdi Ni, Jinjie Qian*, Yongjie Ge, Dong Cai, Huagui Nie, Xuemei zhou*, Zhi Yang*

Key Laboratory of Carbon Materials of Zhejiang Province, Wenzhou University, Wenzhou 325035, China

E-mail: zxm.mei@163.com; jinjieqian@wzu.edu.cn; yang201079@126.com

Experimental section

Synthesis of Ir-NC catalysts

The Ir-NC catalyst was prepared using a top-down synthesis approach. Specifically, 5 mg of Ir(ppy)$_3$ (the structural formula is shown in **Fig. S1**) and 20 mg of CNTs were combined in a mortar and ground uniformly for 30 minutes before being transferred to a tube furnace. The mixture was then heated at a rate of 5 °C min^{-1} until reaching 500 °C, where it was held for 4 hours before naturally cooling. The resulting material was denoted as Ir-NC-500. To facilitate comparative analysis, c-Ir-NC-T samples (c representing initial Ir(ppy)$_3$ content and T denoting annealing temperature) were synthesized by varying the initial iridium content (0.05 wt.%, 0.1 wt.%, 0.15 wt.%) and annealing temperature (300 °C, 500 °C, 700 °C). This was achieved using a similar synthetic procedure as described earlier, with adjustments made to the initial Ir(ppy)$_3$ content and annealing temperature for each sample.

Material characterization

Transmission electron microscopy (TEM), high-resolution TEM (HRTEM), and energy-dispersive X-ray spectroscopy (EDS) elemental mapping analyses were conducted using a JEOL-2100F instrument operating at 200 kV. X-ray diffraction (XRD) patterns were obtained with a D/MAX-2400 diffractometer utilizing Cu Kα radiation (40 kV, 100 mA, λ = 1.54056 Å). X-ray photoelectron spectroscopy (XPS) measurements were performed on an ultrahigh-vacuum setup equipped with a monochromatic Al Ka X-ray source (10 mA, 15 kV) and a high-resolution Gammadata-Scienta SES 2002 analyzer. Raman spectra were captured using a

Renishaw inVia Raman microscope with a 532 nm Ar-ion laser excitation source. Thermogravimetric analysis (TGA) was carried out in an alumina crucible using the simultaneous Thermal Analysis Modulus, SDT Q600 (TA Instruments) controlled by Advantage for Q Series software. The experiment was conducted under an air atmosphere (flow rate of 100 mL min^{-1}) from 40 to 800 $^{\circ}$C at a heating rate of 5 $^{\circ}$C min^{-1}.

Electrochemical characterizations

All the electrochemical tests were performed using a three-electrode system with a saturated calomel electrode (SCE) as the reference electrode and Pt wire as the counter electrode by using a CHI760E electrochemical workstation (CH Instrument Inc). A pre-polished glassy carbon rotating disk electrode (0.196 cm^{-2}) was utilized for ORR in 0.1 M KOH solution, while a mass loading of 0.56 mg cm^{-2} on carbon fiber paper served as the working electrode for OER in 1 M KOH solution. Cyclic Voltammetry (CV) measurements were performed at a scan rate of 10 mV s^{-1}, and Linear scan voltammetry (LSV) measurements were recorded within the potential range of 0.2 to -0.8 V (vs. SCE) for ORR and 0.2 to 0.8 V (vs. SCE) for OER at a scan rate of 10 mV s^{-1}. Electrochemical impedance spectroscopy (EIS) was conducted at open circuit voltage across a frequency range of 0.01 Hz to 100 kHz.

The electron transfer number (n) was determined from LSV curves on a rotating disk electrode (RDE) with varying rotation speeds using the Koutecky-Levich (K-L) equation: $\dfrac{1}{j} = \dfrac{1}{B\sqrt{\omega}} + \dfrac{1}{j_K}$, where j_K is the kinetic current and ω is the electrode rotating

rate. B is determined from the slope of the K-L plots according to the Levich equation as given below: $B = 0.2nFV^{-1/6}C_{O_2}D_{O_2}{}^{2/3}$, where n represents the transferred electron number per oxygen molecule. F is Faraday constant (F = 96485 C mol^{-1}). D_{O_2} is the diffusion coefficient of O_2 in 0.1 M KOH (D_{O_2} = 1.9 × 10^{-5} cm^2 s^{-1}). υ is the kinetic viscosity (υ = 0.01 cm^2 s^{-1}). C_{O_2} is the bulk concentration of O_2 (C_{O_2}= 1.2 × 10^{-6} mol cm^{-3}). The constant 0.2 is adopted when the rotation speed is expressed in rpm.

The $HO_2{}^-$% and transferred electron number per oxygen molecule (n) were determined by the followed equations based on rotating ring-disc electrode (RRDE) measurements: $H_2O_2\% = 200 * \dfrac{I_R/N}{I_D + I_R/N}$ and n=4 x $\dfrac{I_D}{I_D + \dfrac{I_R}{N}}$, where I_D is disk current, I_R is ring current, and N is current collection efficiency of the Pt ring. N was determined to be 0.37.

To extract the apparent activation energy (*Eapp*) of OER, LSV was measured in 1mol KOH solution at different temperatures (35°C, 40°C, 45°C, 50°C, 55°C). For heterogeneous electrocatalytic reactions, the current density can be expressed by the apparent activation energy Eapp in the Arrhenius equation, according to Arrhenius equation: $j = A_{app}\,exp(-\dfrac{E_{app}}{RT})$, A_{app} is the apparent prefactor, R is the ideal gas constant (8.314 J K^{-1}mol^{-1}), and T is the temperature in Kelvin (K). Therefore, it can be further calculated by fitting the slope of the Arrhenius diagram using the equation : $\left|\dfrac{\Delta(ln_{10}j)}{\Delta(1/T)}\right|_\eta = -\dfrac{E_{app}}{R}$.

Fabrication of Zn-air batteries

In the Zn-air battery test, the air electrode was prepared by coating the catalyst ink onto carbon paper (CP) and drying at 40 °C for 6 hours with a mass loading of 5 mg cm^{-2}. The catalyst ink was prepared by mixing 5 mg of catalyst with deionized water, ethyl alcohol, and Nafion under sonication. A Zn plate served as the anode, and both electrodes were assembled into a homemade Zn-air battery using 6 M KOH aqueous solution as the electrolyte. IrO$_2$ and 20 wt% Pt/C in a 1:1 mass ratio were used as control catalysts. Polarization curves were measured at a scan rate of 10 mV s^{-1}. Specific discharge capacity was normalized to the consumed Zn plate mass based on galvanostatic discharge results. The Zn-air battery underwent 300 cycles of 5-minute discharge and 5-minute charge at 10 mA cm^{-2}.
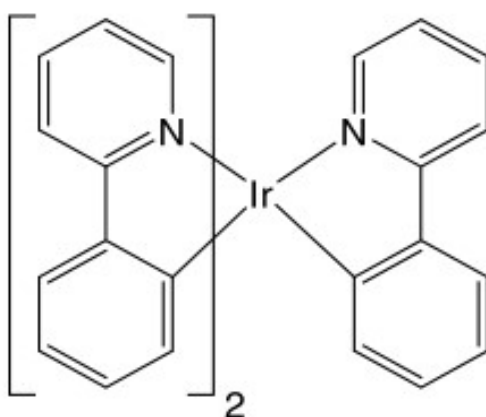
Fig. S1. The molecular structural formula of Ir(ppy)$_3$.
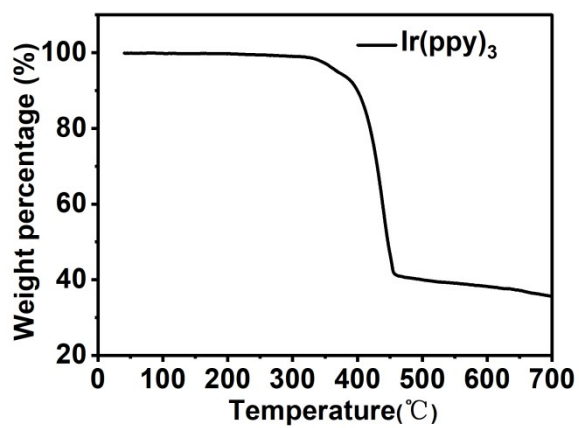
Fig. S2. TGA curves for Ir(ppy)$_3$.
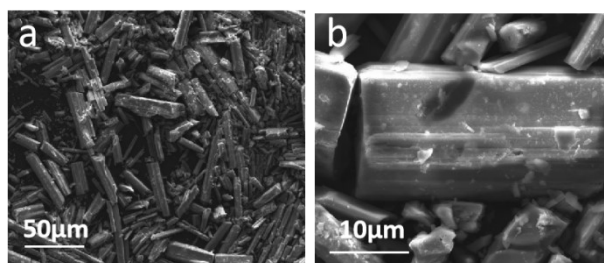
Fig.S3. SEM image of the raw Ir(ppy)$_3$ (a) and Ir(ppy)$_3$-500 without CNTs supports(b).
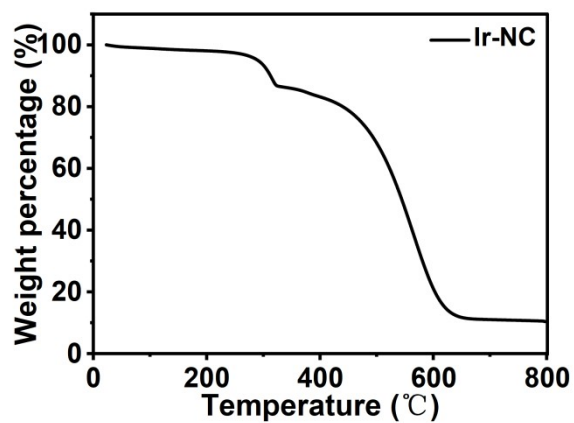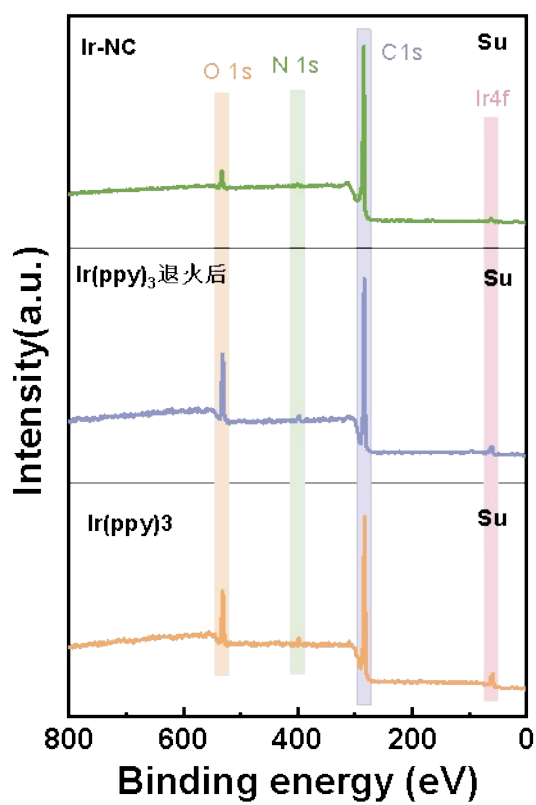
Fig. S4 TGA curves of Ir-NC-500.

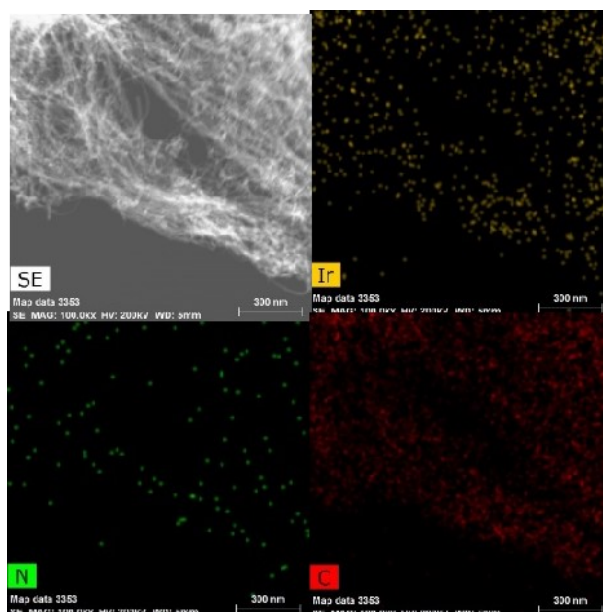**Fig. S5** The full XPS spectroscopy of the Ir(ppy)$_3$、Ir(ppy)$_3$-C、Ir-NC catalyst.

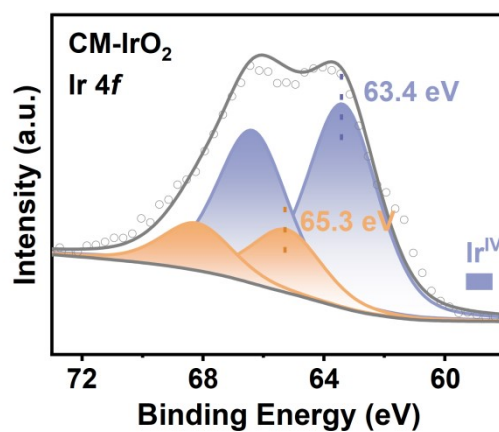**Fig. S6** EDX Mapping (Ir yellow, N green, C red) of the Ir-NC catalyst.
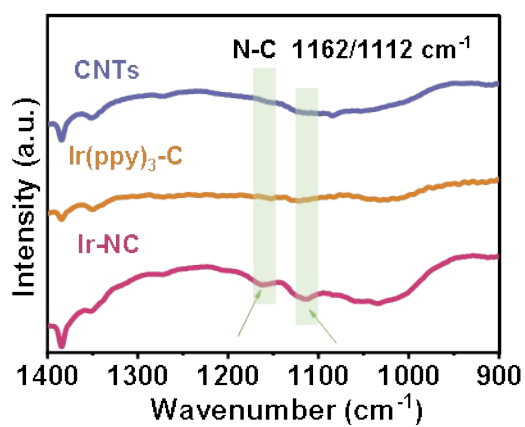

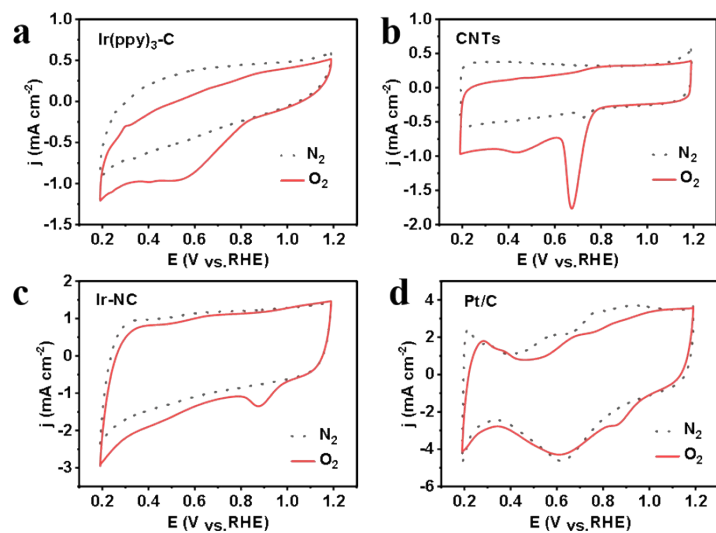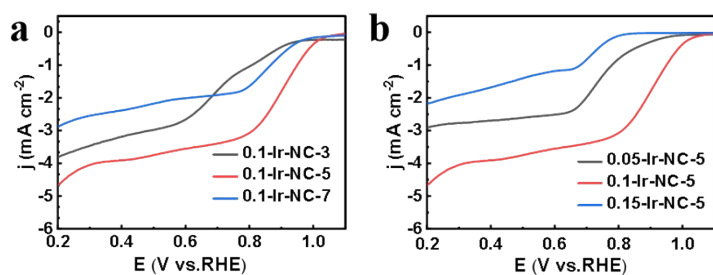**Fig. S7** Ir4f of CM-IrO$_2$.

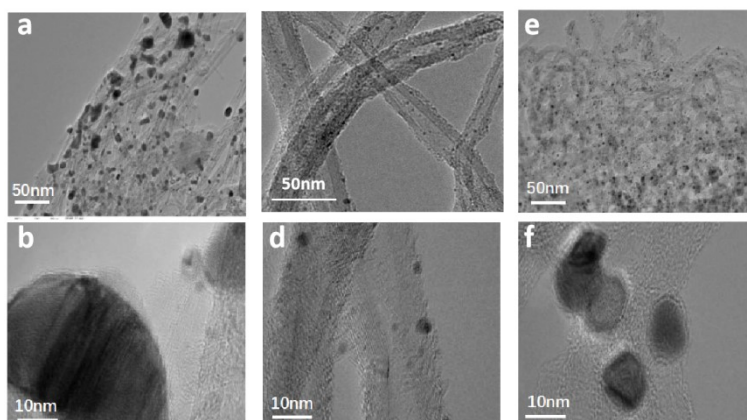**Fig. S8** Infrared images of CNTs, Ir(ppy)$_3$-C, Ir-NC.

Fig. S9 CV curves for CNTs, Ir(ppy)$_3$-C, Ir-NC and Pt/C.

Fig. S10 ORR LSV curves obtained in O$_2$-saturated 0.1 mol L^{-1} KOH at 1600 rmp.

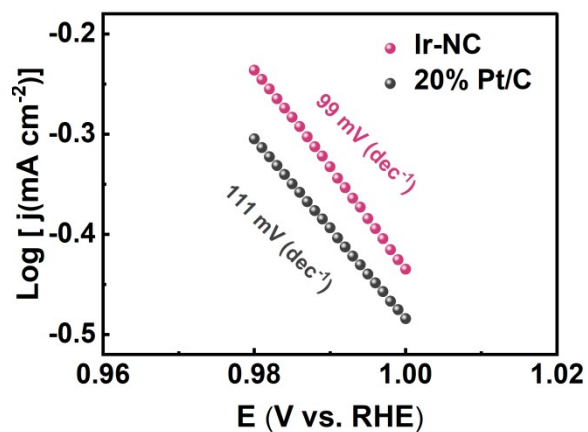**Fig. S11** TEM images of Ir-NC-300 (a, b), Ir-NC-500 (c, d) and Ir-NC-700 (e, f).

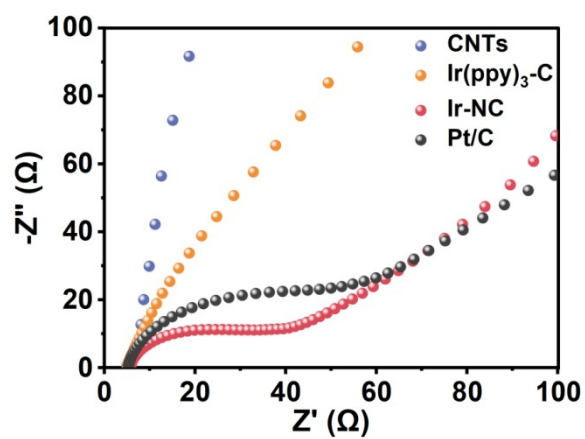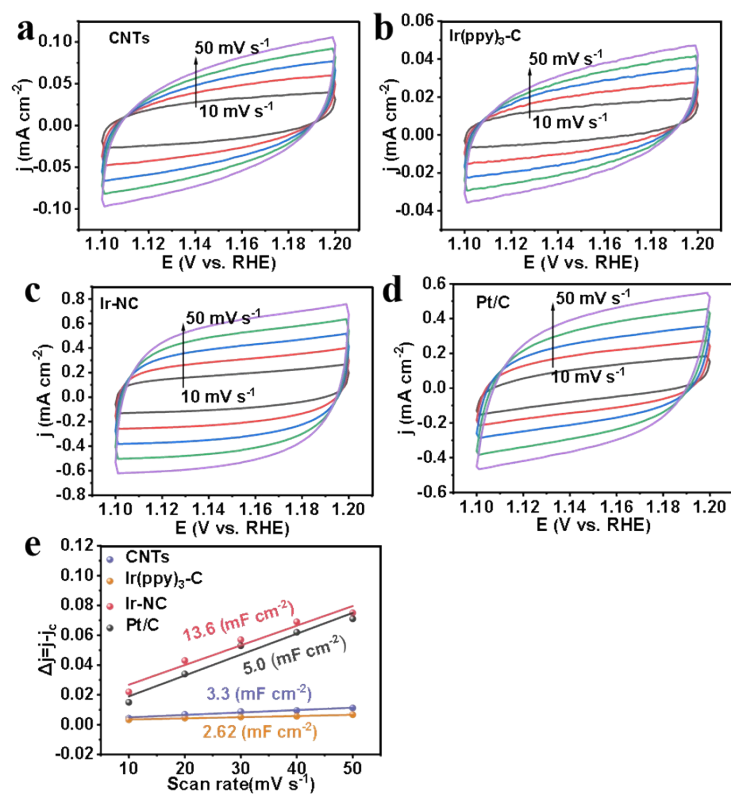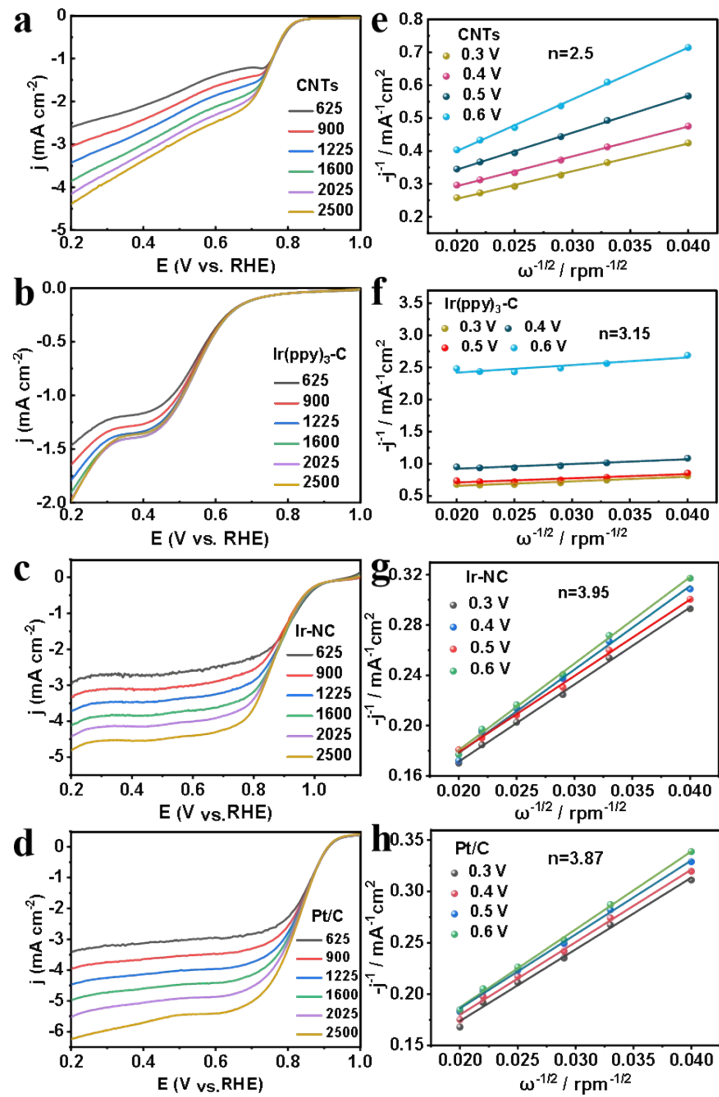**Fig. S12** Tafel slopes of Ir-NC and Pt/C for ORR.

Fig. S13 Nyquist plots at open circuit voltage of CNTs, Ir(ppy)$_3$-C, Ir-NC and Pt/C

Fig. S14. Cycle voltammograms for the (a) CNTs、 (b) Ir(ppy)$_3$-C (c) Ir-NC and d) Pt/C in the non-faradaic capacitance current range at scan rates of 10、 20、 30、 40 and 50 Mv s^{-1} in 0.1M KOH; (e) Charging current density differences plotted versus scan rate. The linear slope, equivalent to twice the double-layer capacitance C_{dl}, was use to represent the ECSA.

Fig. S15. ORR LSV curves at various rotating speeds from 625 to 2500 rpm of (a) CNTs, (b) Ir(ppy)$_3$-Cand (c) Ir-NC and (d) Pt/C in 0.1 M KOH. The K-L plots at various potentials within 0.3-0.6V of (e) CNTs、 (f) Ir(ppy)$_3$-C and (g) Ir-NC and (h) Pt/C.
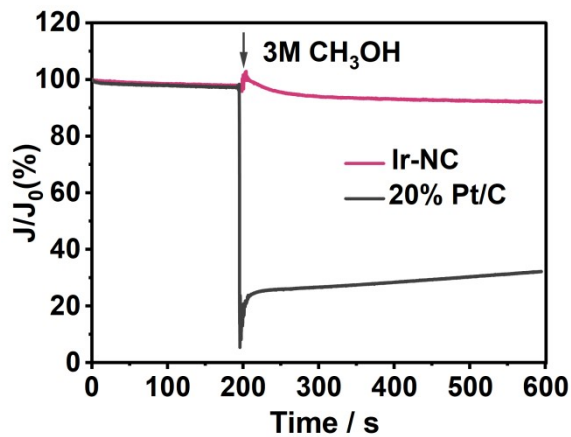
Fig. S16. Chronoamperometric responses of Ir-NC and Pt/C tolerance to carbon monoxide poisoning in oxygen-saturated 0.1 M KOH.

Fig. S17 (a and b) OER LSV curves in 1M KOH.

Fig. S18. Tafel slopes of Ir-NC and CM-IrO$_2$ for OER.
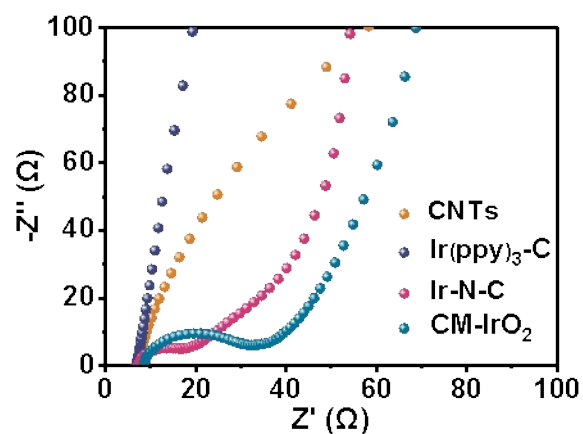
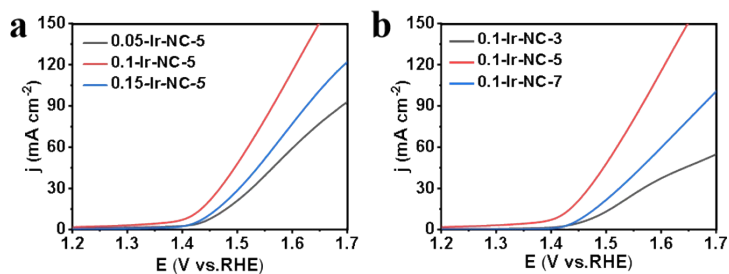**Fig. S19** Nyquist plots at open circuit voltage of CNTs, Ir(ppy)$_3$-C, Ir-NC and CM-IrO$_2$.
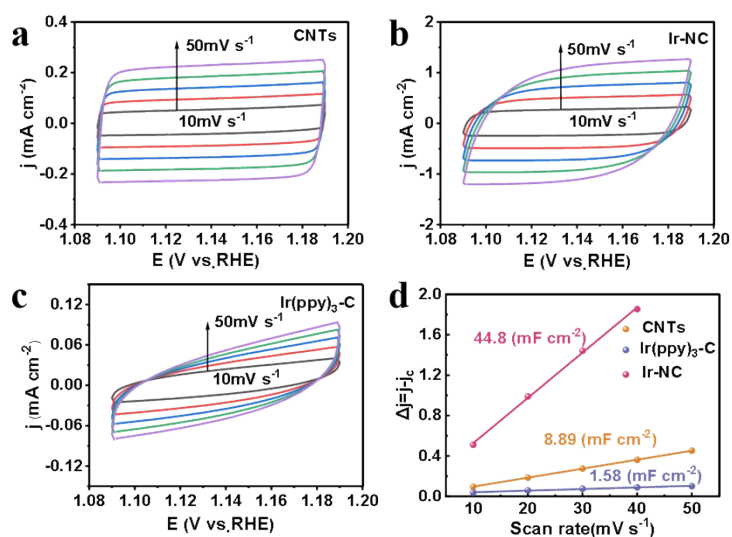
Fig. S20. CVs for the (a) CNTs、(b) Ir(ppy)$_3$-Cand (c) Ir-NC in the non-faradaic capacitance current range at scan rates of 10, 20, 30, 40 and 50 mV s^{-1} in 1 M KOH; (d) Charging current density differences plotted versus scan rate. The linear slope, equivalent to twice the double-layer capacitance C_{dl}, was use to represent the ECSA.
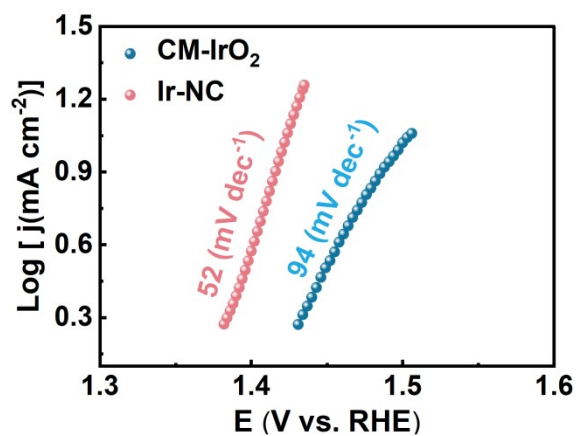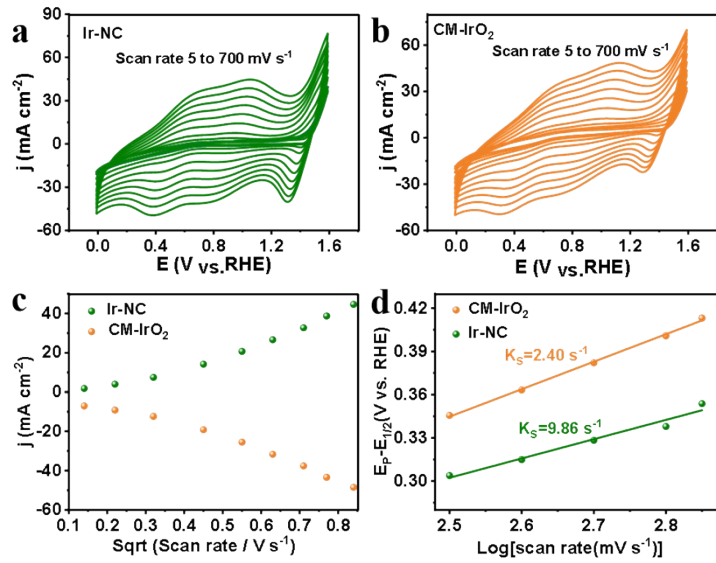
Fig. S21 Electrochemical redox coefficients of Ir-NC (a) and CM-IrO$_2$ (b), (c)The relationship between oxidation current, reduction current and sweep speed square root of Ir-NC and CM-IrO$_2$, (d) Ks of for Ir-NC and CM-IrO$_2$.
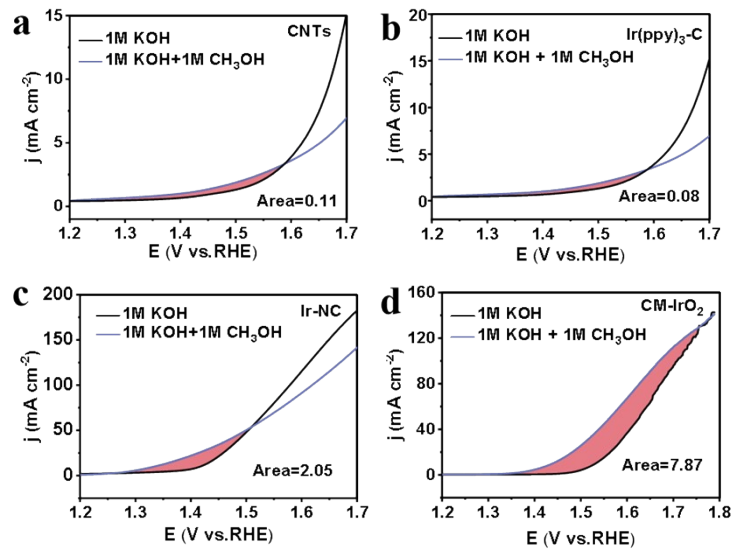
Fig. S22 OER LSV curves for (a) CNTs、 (b) Ir(ppy)$_3$ -C and (c) Ir-NC in 1M KOH in the presence or absence of methanol (1.0 M).
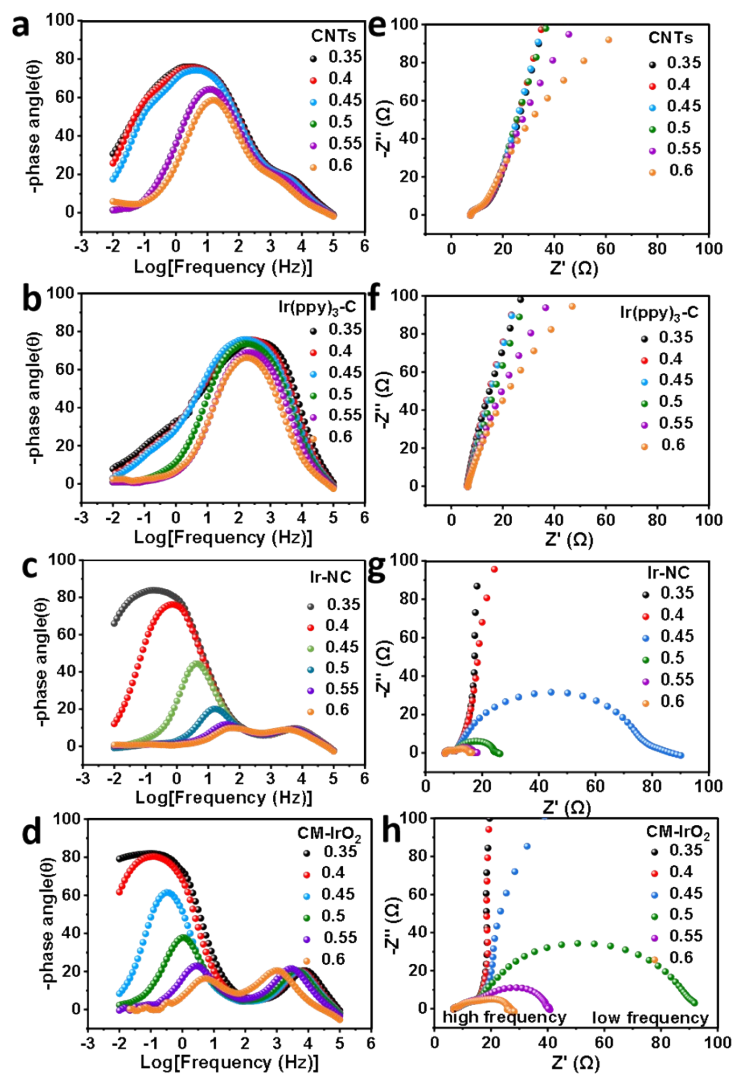
Fig. S23 Nyquist plots and the corresponding Bode absolute impedance plots of (a) CNTs, (b) Ir(ppy)$_3$-C, (c) Ir-NC and (d) CM-IrO$_2$ acquired at 0.35, 0.4, 0.45, 0.5, 0.55, and 0.60 V vs. Hg/HgO, respectively in 1.0 M KOH; (e-h) The c of the same.
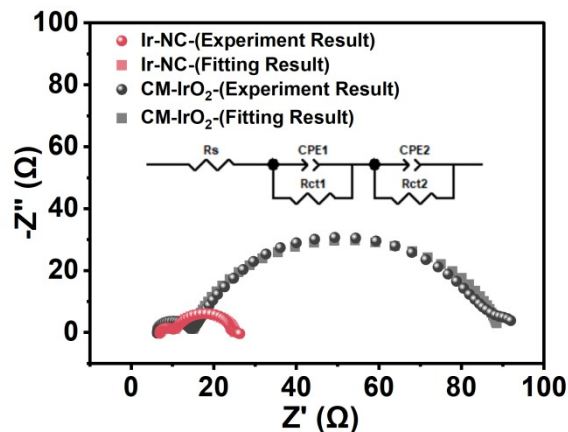
Fig. S24 Nyquist plots of CM-IrO$_2$ and Ir-NC at 0.5 V vs SCE.

Table S3 All values derived from Fig.S21.

Sample	Potential (V vs SCE)	Rs	Rct$_1$	CPE$_1$ (μMho)	Rct$_2$	CPE$_2$ (mMho)
Ir/N-CNTs	0.5	6.92	3.49	47.5	14.72	17.6
CM-IrO$_2$	0.5	6.26	8.61	20.6	74.48	59.0
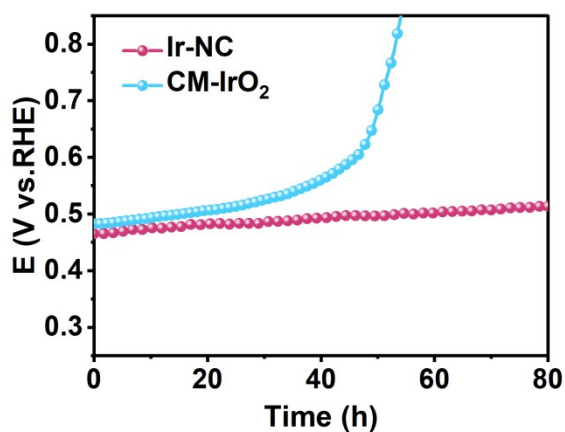
Fig. S25 Electrochemical stability of Ir-NC and CM-IrO$_2$ was measured at the current density of 10 mA cm^{-2}.
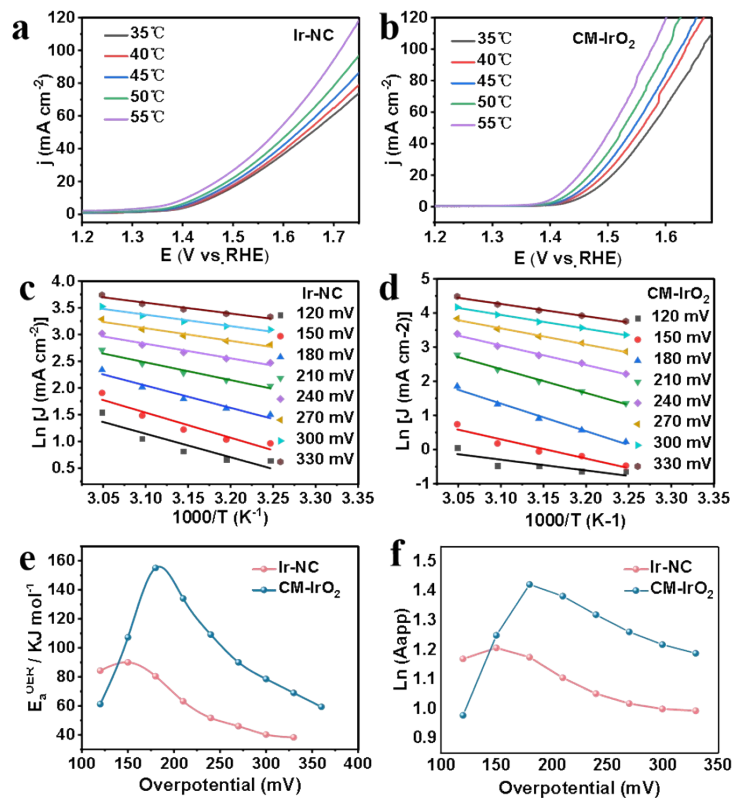
Fig. S26 Temperature-dependent LSVs of (a) Ir-NC and (b) CM-IrO$_2$ measured in 1 M KOH with a sweep rate of 10 mV s^{-1}. Arrhenius plots of (c) Ir-NC and (d) CM-IrO$_2$, respectively, at overpotentials 120, 150, 180, 210, 240, 270, 300 and 330 mV, respectively. (e)The corresponding Eapp data point are calculated from LSV curves recorded at different temperatures (f) The logarithm of pre-exponential factor Aapp derived from the intercept during the extraction of Eapp for Ir-NC and CM-IrO$_2$ catalysts at fixed overpotentials using the Arrhenius plots.
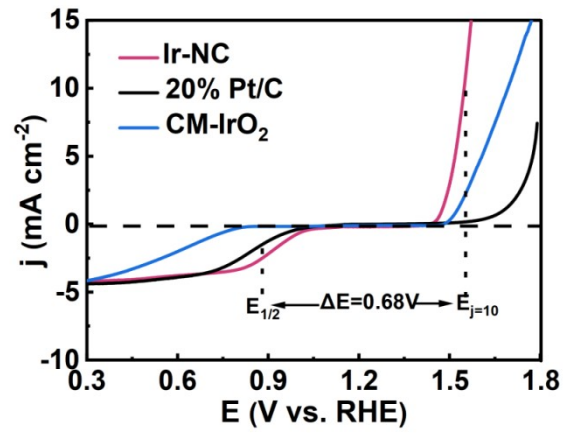
Fig. S27 Bifunctional catalytic activities of electrocatalysts toward ORR and OER.

Fig. S28. The OCP for Ir-NC (a) and Pt/C (b) by measured with a multimeter.
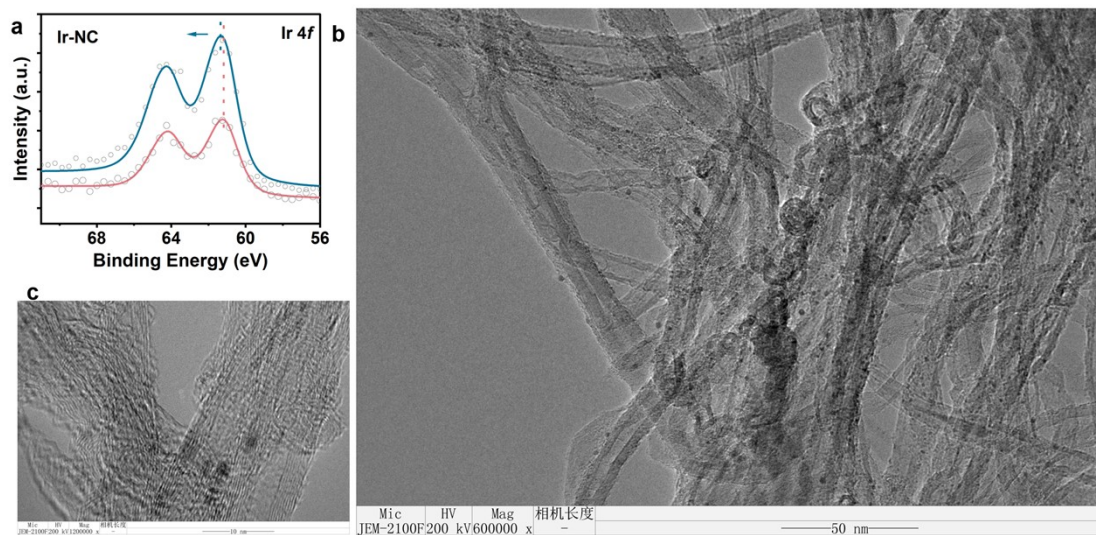
Fig S29. XPS (a) and TEM (b,c) for Ir-NC after the stability test.

Table S1 $E_{1/2}$ values of Ir-NC and Ir-based electrocatalysts towards ORR in 0.1 M KOH

Electrocatalyst	electrolyte	$E_{1/2}$ (V)/η(mV)	Ref.
Ir-NCNT	0.1 M KOH	0.875	This work
mIr NVs	0.1 M KOH	0.873	[1]
Ir@NHCSs	0.1 M KOH	0.76	[2]
Ir/A-rG-O	0.1 M KOH	0.78	[3]
mIrAu NVs	0.1 M KOH	0.893	[1]
Au@Ir CSNWs	0.1 M KOH	0.883	[4]
2%IrO$_2$@CNTs	0.1M KOH	0.796	[5]
	1M KOH	217	
Ir@NG-750	0.1M KOH	0.865	[6]
	1M KOH	273	

Table S2 Comparison of the corresponding overpotential of Ir-NC and othe Ir-based OER catalysts reported at 10 mA cm^{-2} under 1 M KOH.

Electrocatalyst	electrolyte	η(mV) (j=10mA cm^{-2})	Ref.
Ir-NCNT	1 M KOH	188	This work
Ir NSG	1 M KOH	220	[7]
Ir @N-rGO	1 M KOH	260	[8]
Ir@Ni-NDC	1 M KOH	210	
			[9]
Ir@N-G-600	1 M KOH	314	[10]
Ir@N-G-750	1 M KOH	303	[6]

Table S4 Comparison of Zn-air battery performance between Ir-NC and other noble metal electrocatalysts.

Electrocatalyst	OCPT(V)	Power density (mW cm^{-2})	specific capacity (mAh g^{-1}$_{Zn}$) @ xx mA cm^{-2}	Ref
Ir-NCNTs	1.51	157	803@10	This work
SA-Ir/NC	1.42	90.4	776.8 @ 20	[11]
Ir@Co$_3$O$_4$	/	163	712 @ 20	[12]
Pd/Fe-N-C	1.42	/	775 @10	[13]
La$_{0.7}$Sr$_{0.3}$Co$_{0.9}$Pd$_{0.03}$O$_{2.85}$	1.50	52	740 @10	[14]
Pt/NBF-ReS$_2$/Mo$_2$CTx	1.41	180	786@50	[15]
ZIF-67@Pt/CB	1.42	150	/	[16]
CuPt-NC	1.4	253.8	560@20	[17]
SA-PtCoF	1.31	125	808 @10 806@20	[18]
Au@Co$_2$N$_{0.67}$/3D-NGr	1.52	142.8	/	[19]

References

[1] C. Li,Y. Xu,Z. Dai,S. Liu,S. Yu,Z. Wang,X. Li,L. Wang,H. Wang, Bimetallic IrAu mesoporous nanovesicles, Chem. Eng. J. 395 (2020) 125135.

[2] J. Shen,H. Wu,W. Sun,J. Qiao,H. Cai,Z. Wang,K. Sun, In-situ nitrogen-doped hierarchical porous hollow carbon spheres anchored with iridium nanoparticles as efficient cathode catalysts for reversible lithium-oxygen batteries, Chem. Eng. J. 358 (2019) 340-350.

[3] K. Choi,S. Lee,Y. Shim,J. Oh,S. Kim,S. Park, Electrocatalytic performances of N-doped graphene with anchored iridium species in oxygen reduction reaction, 2D Materials. 2 (3) (2015) 034019.

[4] Q. Xue,H.-Y. Sun,Y.-N. Li,M.-J. Zhong,F.-M. Li,X. Tian,P. Chen,S.-B. Yin,Y. Chen, Au@Ir core-shell nanowires towards oxygen reduction reaction, Chem. Eng. J. 421 (2021) 129760.

[5] X. Wen,L. Bai,M. Li,J. Guan, Ultrafine iridium oxide supported on carbon nanotubes for efficient catalysis of oxygen evolution and oxygen reduction reactions, Materials Today Energy. 10 (2018) 153-160.

[6] Q. Zhang,Z. Duan,Y. Wang,L. Li,B. Nan,J. Guan, Atomically dispersed iridium catalysts for multifunctional electrocatalysis, J. Mater. Chem. A. 8 (37) (2020) 19665-19673.

[7] Q. Wang,C.-Q. Xu,W. Liu,S.-F. Hung,H. Bin Yang,J. Gao,W. Cai,H. M. Chen,J. Li,B. Liu, Coordination engineering of iridium nanocluster bifunctional electrocatalyst for highly efficient and pH-universal overall water splitting, Nat. Commun. 11 (1) (2020) 4246.

[8] W. Yao,X. Jiang,Y. Li,C. Zhao,L. Ding,D. Sun,Y. Tang, N-doped graphene anchored ultrasmall Ir nanoparticles as bifunctional electrocatalyst for overall water splitting, Green Energy Environ. 7 (5) (2022) 1111-1118.

[9] J. Yang,Y. Shen,Y. M. Sun,J. H. Xian,Y. J. Long,G. Q. Li, Ir Nanoparticles Anchored on Metal-Organic Frameworks for Efficient Overall Water Splitting under pH-Universal Conditions, Angew. Chem. Int. Ed. 62 (17) (2023).

[10] L. Yi,B. Feng,N. Chen,W. Li,J. Li,C. Fang,Y. Yao,W. Hu, Electronic interaction boosted electrocatalysis of iridium nanoparticles on nitrogen-doped graphene for efficient overall water splitting in acidic and alkaline media, Chem. Eng. J. 415 (2021) 129034.

[11] X. Luo,M. Yang,W. Song,Q. Fang,X. Wei,L. Jiao,W. Xu,Y. Kang,H. Wang,N. Wu,W. Gu,L. Zheng,L. Hu,C. Zhu, Neutral Zn-Air Battery Assembled with Single-Atom Iridium Catalysts for Sensitive Self-Powered Sensing System, Adv. Funct. Mater. 31 (24) (2021) 2101193.

[12] Y. Dai,J. Yu,J. Wang,Z. Shao,D. Guan,Y.-C. Huang,M. Ni, Bridging the Charge Accumulation and High Reaction Order for High-Rate Oxygen Evolution and Long Stable Zn-Air Batteries, Adv. Funct. Mater. 32 (24) (2022) 2111989.

[13] J. Chen, Z. Wang, C. Yang, G. Zou, S. Liu, Z. Sun, L. Wang, R. Li, K. Qu, W. Kang, Electrocatalytic Oxygen Reduction Reaction by the Pd/Fe-NC Catalyst and Application in a Zn–Air Battery, Catalysts 12 (2022) 1640.

[14] R. Majee,T. Das,S. Chakraborty,S. Bhattacharyya, Shaping a Doped Perovskite Oxide with Measured Grain Boundary Defects to Catalyze Bifunctional Oxygen Activation for a Rechargeable Zn–Air Battery, ACS Appl. Mater. Interfaces. 12 (36) (2020) 40355-40363.

[15] M. Yi,N. Li,B. Lu,L. Li,Z. Zhu,J. Zhang, Single-atom Pt decorated in heteroatom (N, B, and F)-doped ReS_2 Grown on Mo_2CTx for efficient pH-universal hydrogen evolution reaction and flexible Zn–air batteries, Energy Storage Materials. 42 (2021) 418-429.

[16] J. Li,Z. Meng,D. J. L. Brett,P. R. Shearing,N. T. Skipper,I. P. Parkin,S. Gadipelli, High-Performance Zinc–Air Batteries with Scalable Metal–Organic Frameworks and Platinum Carbon Black Bifunctional Catalysts, ACS Appl. Mater. Interfaces. 12 (38) (2020) 42696-42703.

[17] V. M. Dhavale,S. Kurungot, Cu–Pt Nanocage with 3-D Electrocatalytic Surface as an Efficient Oxygen Reduction Electrocatalyst for a Primary Zn–Air Battery, ACS Catal. 5 (3) (2015) 1445-1452.

[18] Z. Li,W. Niu,Z. Yang,N. Zaman,W. Samarakoon,M. Wang,A. Kara,M. Lucero,M. V. Vyas,H. Cao,H. Zhou,G. E. Sterbinsky,Z. Feng,Y. Du,Y. Yang, Stabilizing atomic Pt with trapped interstitial F in alloyed PtCo nanosheets for high-performance zinc-air batteries, EES. 13 (3) (2020) 884-895.

[19] D. C. Nguyen,T. L. L. Doan,S. Prabhakaran,D. H. Kim,N. H. Kim,J. H. Lee, Rational construction of $Au@Co_2N_{0.67}$ nanodots-interspersed 3D interconnected N-graphene hollow sphere network for efficient water splitting and Zn-air battery, Nano Energy. 89 (2021) 106420.